Journal of Colloid and Interface Science 562 (2020) 29–41

Contents lists available at ScienceDirect

Journal of Colloid and Interface Science

journal homepage: www.elsevier.com/locate/jcis

Highly selective surface adsorption-induced efficient photodegradation of cationic dyes on hierarchical ZnO nanorod-decorated hydrolyzed PIM-1 nanofibrous webs

Kugalur Shanmugam Ranjith [a,b,*], Bekir Satilmis [a,c], Yun Suk Huh [d], Young-Kyu Han [b,*], Tamer Uyar [a,e,*]

[a] Institute of Materials Science & Nanotechnology, Bilkent University, Ankara 06800, Turkey
[b] Department of Energy and Material Engineering, Dongguk University, Seoul 04620, Republic of Korea
[c] Department of Medical Services and Techniques, Vocational School of Health Services, Kirsehir Ahi Evran University, Kirsehir 40100, Turkey
[d] Department of Biological Engineering, Inha University, Incheon 22122, Republic of Korea
[e] Department of Fiber Science & Apparel Design, Cornell University, Ithaca, NY 14853, United States

GRAPHICAL ABSTRACT

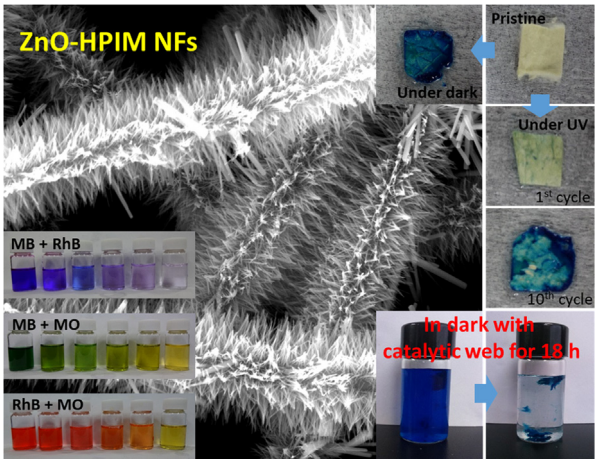

ARTICLE INFO

Article history:
Received 9 September 2019
Revised 22 November 2019
Accepted 23 November 2019
Available online 25 November 2019

Keywords:
Electrospinning
Polymers of intrinsic microporosity (PIMs)
HPIM-ZnO nanofibers
Hierarchical fibrous web

ABSTRACT

Selectivity of catalysts toward harmful cationic pollutants in industrial wastewater remains challenging but is of crucial importance in environmental remediation processes. Here, we present a complex network of a hydrolyzed polymer of intrinsic microporosity (HPIM)-based electrospun nanofibrous web with surface functional decoration of ZnO nanorods (NRs) as a hierarchical platform for selective and rapid degradation of cationic dyes. Over a single species or binary mixtures, cationic dyes were selectively adsorbed by the HPIM surface, which then rapidly degraded under simultaneous photoirradiation through the ZnO NRs. Both HPIM and ZnO exhibited high electronegative surfaces, which induced the selectivity towards the cationic dyes and rapidly degraded the pollutants with the production of reactive oxygen species under photoirradiation. Further, as a free-standing web, the catalytic network could be easily separated and reused without any significant loss of catalytic activity after multiple cycles of

* Corresponding authors at: Institute of Materials Science & Nanotechnology, Bilkent University, Ankara 06800, Turkey (K.S. Ranjith and T. Uyar).
E-mail addresses: ranjuphy@gmail.com (K.S. Ranjith), ykenergy@dongguk.edu (Y.-K. Han), tu46@cornell.edu (T. Uyar).

https://doi.org/10.1016/j.jcis.2019.11.096

Cationic dye adsorption
Photodegradation

use. The hierarchical platform of ZnO/HPIM-based heterostructures could be a promising catalytic template for selective degradation of synthetic dyes in mixed wastewater samples.

1. Introduction

Designing the hierarchical form of a catalytic membrane with high adsorption capacity and selectivity towards the degradation of toxic industrial effluents, organic pollutants, and their derivatives are crucial in environmental remediation processes to ensure human health and environmental protection [1,2]. Even at low concentrations, these pollutants are genotoxic and disrupt the endocrine system, posing a hazard to human health. Cationic dyes such as methylene blue (MB) and rhodamine B (RhB), frequently used in textiles and printing-based industries, are highly detrimental to the ecosystem [3]. Effluent from these industries contaminates the environment, by not only coloring the water bodies but also affecting the aquatic life by reducing the dissolved oxygen level and blocking the entry of sunlight into water [4,5]. Many studies have investigated removing and degrading organic pollutants from industrial waste using methods such as filtration [6,7], adsorption [8], degradation [9], and chemical oxidation [10,11]. Selective filtration or degradation of toxic components in mixed aqueous waste samples have, however, proven challenging. It is thus necessary to prepare a catalyst that offers effective degradation and selectivity towards the pollutants in the mixed aqueous solution at a low cost with effective stability and reusability [12]. Potential surfaces for the effective removal of pollutants from the water body and air are in high demand. Substrates that are used for effective adsorption cannot degrade those pollutants and offer limited adsorption capacity [13–15]. Different semiconducting nanostructures have, however, exhibited promising potential in degrading organic pollutants but they do not exhibit selectivity towards specific pollutants [16–18]. However, semiconducting nanostructures require photon energy to degrade the dye and organic molecules and do not show any notable activity toward the pollutants in the dark. In order to improve their functionality, active catalytic metal oxide nanostructures have been attached to appropriate supports offering the capacity for effective adsorption, which increases the possibility of interactions with the photogenerated carrier to degrade the pollutant ions [19,20]. Mostly, graphene and carbon-based supports are used in hybridization with semiconducting nanostructures to improve the catalytic activity and dye interactions toward the catalytic process [21–23]. Apart from carbon-based supports, some polymer-based functional surfaces have been employed together with semiconducting nanostructures to promote effective degradation under photoirradiation.

Polymers of intrinsic microporosity (PIMs) are a new class of polymers that attracted significant interest: they exhibit selectivity toward the detection of certain organic compounds through their surface functionality. Modifying the structural functionality of PIM-1, the first synthesized PIM polymer, in the form of hydrolyzed PIM-1 (HPIM) allowed it to adsorb cationic dye molecules such as methylene blue (MB) and methylene violet (MV), but it did not adsorb the anionic compound methyl orange (MO) [24,25]. Furthermore, PIM-I nanofeatures with additional functional surface features allowed uranium adsorption on it unlike on the parent PIM surface [26]. In addition, the fibrous assembly of PIMs showed better adsorption performance than their dense film surfaces [27–29]. Recent developments in the field have revealed the advantages of electrospun nanofibers (NFs) and membrane/web-based catalysts, which are considered the most effective materials due to their simple recovery and reusability features. PIM-1 exhibits excellent solubility in common organic solvents and it could be simply modified by hydrolysis in the presence of sodium hydroxide resulting in hydrolyzed PIM-1 (HPIM), which displays selectivity towards cationic dye molecules leading to advantageous selective filtration of textile pollutants from mixed aqueous solutions [24]. HPIM has shown high selectivity toward adsorption of certain species as a catalyst, with easy reusability that makes it feasible for real-time applications. Easy handling of the catalyst for multiple uses is possible if specific steps to extract the adsorbed species can be ensured or if it is tethered to an immobilized template. Tagging magnetic species to the semiconductor has led to easy extraction after catalytic activity [30,31], but this was enabled only by a few transition metal-based semiconducting nanostructures. Tagging the catalyst in a membrane or preparing the catalyst as a membrane provides in the opportunity for reusability and easy handling. Ranjith et al. [32] have reported the atomic layer deposition of monodisperse Pd nanograins on a polymeric web for effective and reusable catalytic activity. Immobilizing the catalyst on the polymeric web improved the reusability. Polymeric nanofibers played the role of a membrane and exhibited effective and selective adsorption toward different pollutants in a mixed sample [33,34]. In general, wide bandgap semiconductors such as TiO_2 and ZnO are considered promising photocatalysts because of their high redox potential toward photogenerated charge carriers. The nontoxicity, affordability, and high electron mobility, however, hinder ZnO from being suitable as an alternative to TiO_2 [35–37]. Fatma et al. [38] have decorated a polymer fibrous web with ZnO nanorods (NRs): the resulting system revealed effective and stable catalytic performance under UV irradiation and was reusable. Constructing a hierarchical platform with a polymer–semiconductor heterostructure could improve the selectivity and degradation toward cationic dyes, which would offer great potential in environmental remediation applications.

Herein, we intended to design a hierarchical ZnO NR-decorated HPIM electrospun nanofibrous web offering adsorption of cationic dyes through favorable selective surface interactions followed by degradation from mixed aqueous wastewater samples. We demonstrate a hierarchical design of a free-standing catalytic web exhibiting selective adsorption towards cationic dyes with high activity that was easily recoverable and reusable. To our knowledge, we are the first to report the effective and selective degradation of organic pollutants on a hierarchical membrane surface comprising ZnO on a HPIM NF surface.

2. Experimental section

2.1. Materials

5,5′,6,6′-Tetrahydroxy-3,3,3′,3′-tetramethyl-1,1′-spirobisindane (TSBI, 98%, Alfa Aesar), Tetrafluoroterephthalonitrile (TFTN, 97%, Alfa Aesar), anhydrous potassium carbonate (K_2CO_3, 99.0%, Alfa Aeser), sodium hydroxide (NaOH, pellets), N—N, dimethylformamide (DMF, ≥99.8%), ethanol (EtOH, ≥99.8%), toluene (99.9%), dimethylacetamide (DMAc, ≥99.9%), chloroform ($CHCl_3$, 99–99.4%), and methanol (MeOH, ≥99.8%) were obtained from Sigma Aldrich. Atomic layer deposition (ALD) of ZnO was performed using diethylzinc (DEZN, Sigma-Aldrich) and HPLC-grade water (H_2O) as the zinc precursor and oxidant, respectively. For

ZnO NR growth, zinc nitrate hexahydrate (≥98%, Sigma-Aldrich) and hexamine (≥99%, HMTA, Alfa Aesar) were used. Methylene blue (MB, Sigma-Aldrich), rhodamine B (RhB, Sigma-Aldrich), and methyl orange (MO, Sigma-Aldrich) were used as model pollutants. All the chemicals were used as received without any further purification. De-ionized (DI) water was obtained from a Millipore Milli-Q system.

2.2. Synthesis of HPIM

The parent PIM-1 was synthesized by reacting TSBI and TFTN monomers according to a reported procedure [39]. Hydrolysis of PIM-1 was achieved as reported previously [24]. Briefly, 1 g of PIM-1 powder was reacted with NaOH (25% *w*/*v*) in the presence of H_2O/EtOH (1:1) at 120 °C for 3 h. Then, DI water (100 mL) was added to this solution prior to filtration under vacuum and dried at 110 °C overnight. The dried sample was placed in acidic water (pH = ~4) for 2 h and the mixture was filtrated and washed with water and then dried at 110 °C overnight.

2.3. Electrospinning of HPIM nanofibrous web

Electrospinning of HPIM powder was achieved according to a previously reported procedure [24]. Briefly, 70% w/v HPIM powder was dissolved in DMF at room temperature and stirred for 5 h. The solution was loaded in a 1 mL syringe equipped with a blend needle with an outer diameter of 1.2 mm and placed on a syringe pump (K_D Scientific, KDS 101). An aluminum foil-coated metal plate was used as the collector using the following parameters: 0.5 mL h^{-1} flow rate, 12 kV applied voltage, and 15 cm distance between collector and needle. The fibrous web thus obtained was detached from the aluminum foil and dried at 110 °C under vacuum overnight.

2.4. Decoration of ALD-grown ZnO nanograins on HPIM surface

The electrospun HPIM nanofibrous web was used as a substrate in an ALD process to deposit ZnO nanograins on the surface at 200 °C in a Savannah S100 ALD reactor (Cambridge Nanotech Inc.). N_2 was used as a carrier gas at a flow rate of 20 sccm. 100 cycles of ZnO were applied in the exposure mode to attain a monodisperse dense nanograin assembly that offered a nucleation layer for ZnO NR growth. DEZn precursor and H_2O were used as counter reactants. The following parameters were used for each cycle of ALD: valve OOF/N_2 flow set to 10 sccm/H_2O pulse (0.015 s)/exposure (10 s)/valve ON/N_2 purge (20 sccm, 10 s) valve OFF/N_2 flow set to 10 sccm/DEZn pulse (0.015 s)/exposure (10 s) calve ON/N_2 purge (200 sccm, 10 s). After the ALD process, ZnO-seeded HPIM NFs were annealed at 250 °C in air for 2 h.

2.5. ZnO NR growth on HPIM NF surface

The ALD-processed ZnO-seeded HPIM nanofibrous web was used as a substrate for ZnO NR growth in a low-temperature aqueous solution growth process.[37] 125 mM of zinc nitrate and 125 mM of HMTA were dissolved to form separate UV-treated Millipore water solutions and vigorously stirred for 10 min; the HMTA solution was then added dropwise to the zinc nitrate solution to attain a single-phase solution. The ALD-processed seed-decorated electrospun HPIM nanofibrous web was tagged with the glass substrates and immersed into the growth solution without letting it touch the ground. The reaction was maintained at 97 °C for 6 h and the solution was gently stirred throughout the growth process. After completing the growth process, the ZnO NR-decorated HPIM nanofibrous web was cleaned twice with Millipore water and dried at 150 °C for 30 min.

2.6. Characterization

The surface features and surface morphology of the nanofibrous web were analyzed by scanning electron microscopy (SEM, FEI-Quanta 200 FEG) and transmission electron microscopy (TEM, FEI–Tecnai G2F30) equipped with energy-dispersive X-ray spectroscopy (EDAX). The structural properties were analyzed using X-ray diffraction (XRD, PANalytical X'Pert Multipurpose X-ray diffractometer with Cu K radiation (λ = 0.15418 nm)). X-ray photoelectron spectroscopy (XPS) was performed with a Thermo K-alpha-monochromated spectrometer in the constant analyzer energy mode. Fourier transform infrared (FT-IR) spectra were obtained using a Jasco FT/IR-6600 unit using KBr pellets from 4000 to 400 cm^{-1}. A TA Q500 instrument was employed for thermogravimetric analysis (TGA) to investigate the thermal properties of the samples, which were heated to 600 °C at 20 °C min^{-1} in a N_2 atmosphere. ^{1}H nuclear magnetic resonance (^{1}H NMR) spectra were obtained using a Bruker DPX-400 MHz spectrometer at room temperature in d_6-DMSO. The diffuse reflectance spectra (DRS) of nanocatalytic arrays were obtained using a UV–visible spectrophotometer (UV–Vis, Jasco V-770). Zeta potentials of the HPIM- and ZnO-nanorod-dispersed solution were determined by a Brookhaven Instruments ZetaPALS DB-525 instrument. Each sample was measured in triplicate during zeta potential measurements, and experimental results refer to the average values. Photoluminescence (PL) measurements were performed using an FL-1057 time-resolved fluorescence spectrophotometer.

2.7. Dye adsorption and degradation

Photocatalytic activity of the samples was estimated by monitoring the decomposition of MB, MO, RhB dyes, and the mixed phase under UV irradiation (ULTRA VIYALUX UV-A, 300 W, Osram) at room temperature. The ZnO-HPIM based catalytic web with dimensions of 1 cm × 1 cm was immersed in 5 mL of a 15-ppm dye solution (pH: 6.3) in a quartz cuvette. Quartz cuvettes with different compositions (pristine HPIM, ALD-processed HPIM, and ZnO NR-decorated HPIM) of the nanofibrous web were placed side by side and simultaneously irradiated by UV light. As a control experiment, a dye solution without any catalyst and ZnO NR-decorated PAN NFs were subjected to the same photo treatment for comparison with the ZnO NR-decorated HPIM NFs. At specific time intervals, the concentration of the dyes was recorded by measuring the absorbance of the solution at 661 nm, 456 nm, and 542 nm for MB, MO, and RhB respectively, using a Jasco V-770 spectrophotometer. All the mentioned experiments were performed in neutral conditions (pH: 6.3) and further, the catalytic activity was also studied as a function of the pH of the solution, which was controlled by adding HCl and NaOH to vary the pH between 3 and 11. The concentration of organic dyes was determined by measuring the adsorption intensity at the maximum absorbance wavelength of the supernatant and the degradation percentage (η) of the solutions was quantified [39]. To understand the effective role of the adsorption efficiency of nanofibrous surface, the samples were kept in darkness and the adsorption efficiency was quantified against time. The hierarchical fibrous structure attained adsorption equilibrium in the dark but simultaneous adsorption followed by photodegradation effectively induced the destruction of the adsorbed pollutant, which maximized the dye loading capability under UV irradiation. Further, the effective adsorption and degradation of dye functionalities on the nanofibrous surface were analyzed using FT-IR and UV DRS spectra. The reusability was studied over ten consecutive cycles to test the stability of the photocatalysts. The detailed experimental procedure and calculations are given in Supporting Information.

3. Results and discussion

Synthesis of HPIM powder and electrospinning of free-standing HPIM fibrous membrane were performed according to our previous report [29]. The FT-IR and ^{1}H NMR spectra and TGA curve of the HPIM powder are provided in Fig. S1. PIM-based materials exhibit selective functionality suitable for adsorption and thus they have been used in filtration-based applications depending on their functionalities in the form of a nanofibrous web. The fibrous free-standing membrane has driven a range of innovative functionalities on PIM-based materials unlike for its powder and film forms [24,39]. Recent reports have evidenced selective cationic adsorption (of the MB dye) by the hydrolyzed PIM-based nanofibers and its effective filtration of dye molecules from the wastewater in the fibrous membrane form [24]. The adsorbate will not be a perfect solution for water treatment, but degradation of the adsorbed pollutant will be a key solution toward effective wastewater management. In this study, we decorated ZnO on the HPIM surface to degrade selectively adsorbed pollutants under photoirradiation in a simultaneous adsorption-cum-degradation process. Decorating ZnO on hydrophobic HPIM surface was highly challenging and initiated the random growth of ZnO nanofeatures in unseeded and solution-based seeding processes (Fig. S2 & S3). To overcome this process, we induced the HPIM as a substrate in the ALD process and decorated a monodisperse uniform assembly of ZnO nanograins, which acted as a nucleation platform for the growth of ZnO NRs on the HPIM nanofiber surface. ALD offers physical interactions with monodisperse ZnO nanograins throughout the fibrous network and initiates ZnO NR growth on the HPIM fiber surface.

The schematic assembly of the obtained hierarchical form of the nanofibrous web is shown in Fig. 1. Controlled, post-optimized growth conditions have paved a way to the preparation of hierarchical form of ZnO NR-decorated electrospun HPIM nanofibers [40]. Fig. 2 clearly reveals the morphological evolution of the HPIM surface after the ALD and solution growth processes. Fig. 2a and b shows the low- and high-magnification SEM images of the electrospun HPIM nanofibers. The HPIM fibers had a uniform diameter of ~1 μm with a free-standing web finish with a hydrophobic nature (inset, Fig. 2**b**) [41]. Solution phase ZnO nucleation on HPIM fibers resulted in poor interaction and offered irregular ZnO NR growth in the form of patches (Fig. S3) due to the hydrophobicity.

In the ALD process, the HPIM exhibited structural stability without undergoing destruction of its fibrous morphology (Fig. 2c, d). HPIM fibers showed thermal stability at a temperature of nearly 250 °C (Fig. S4) and could withstand the deposition temperature of ALD (200 °C). Using ALD, a ZnO nucleation (seed layer) was decorated on the HPIM nanofibers to grow ZnO NRs on the fiber surface as a hierarchical assembly (Fig. 2e). The grown ZnO NR arrays had an average length of 1.5 μm with a uniform diameter of 50–70 nm (Fig. 2f). After the hierarchical ZnO NR growth, HPIM NFs retained their hydrophobic nature. During the ZnO NR growth on the HPIM surface, while the ALD-free ZnO nucleation resulted in a random distribution of microstructural growth of ZnO NRs with poor surface interaction (Fig. S2). Fig. 3(a–d) shows the coverage of the ALD-processed ZnO seed layers and the ZnO NR growth on the HPIM fiber surface as determined by TEM investigation. Under the ALD process at the deposition temperature of 200 °C, a semi-conformal monodisperse nanograin assembly of a dense ZnO base thin layer was observed (Fig. 3a). The resulting bright contracted nanograins on the HPIM surface evidenced ZnO nuclei of a spherical shape with sizes of 3–6 nm (Fig. 2b). The nanograins were in the polycrystalline phase, which favored post-growth of ZnO NRs on the HPIM surface. EDAX (Fig. S5) of HPIM nanofibers confirmed the presence of ZnO on the surface. Fig. 3c shows the ZnO NR growth on the HPIM surface with growth initiation from the ALD seed surface, which acted as a nucleation platform. The high-magnification TEM images of the ZnO NRs exhibit a NR diameter of around 50 nm that were nearly vertically aligned to the fiber surface.

Fig. 4 displays the XRD pattern of HPIM fibers and ZnO-decorated HPIM. The XRD pattern of the pristine HPIM nanofibers exhibited only the carbon-based spectral peak. Integrating ZnO nanograins through the ALD process led to peaks at 2θ = 32.4°, 34.6°, and 36.5°, which represent the (1 0 0), (0 0 2), and (1 1 0) peaks and clearly matched those of the hexagonal wurtzite crystal structure (ICDD 01-074-9940) of ZnO [38]. This suggests the successful deposition of ZnO on the HPIM surface after the ALD process. On the ZnO NR-decorated HPIM surface, the intensity of the ZnO based peaks increased, suggesting the density of ZnO sites

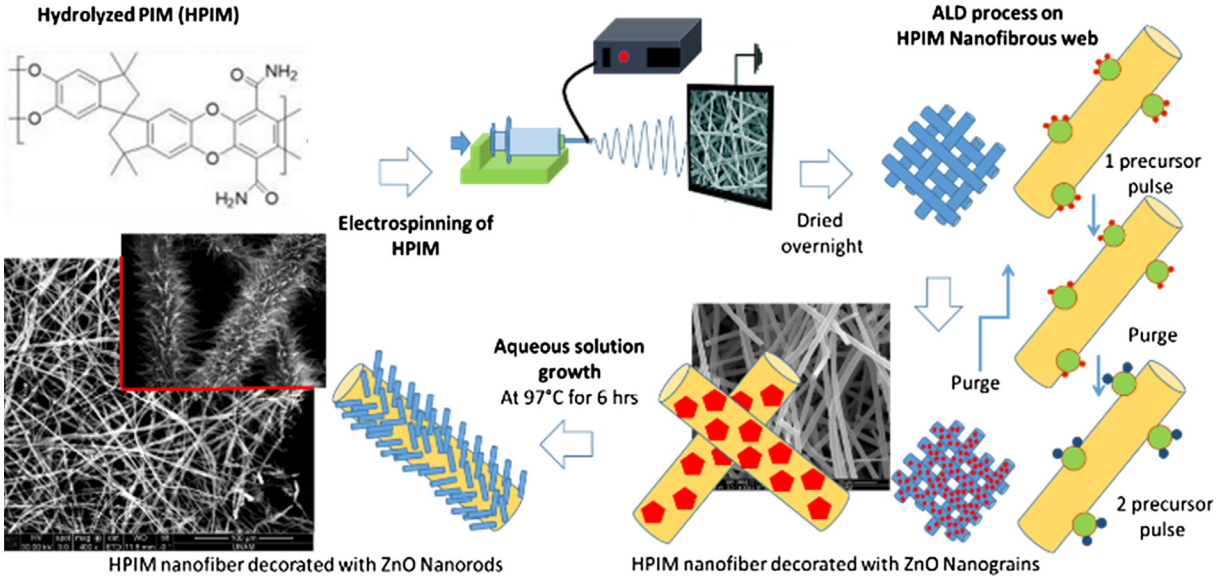

Fig. 1. Schematic illustration of growth process of hierarchical assembly of ZnO NR-decorated HPIM electrospun nanofibrous web.

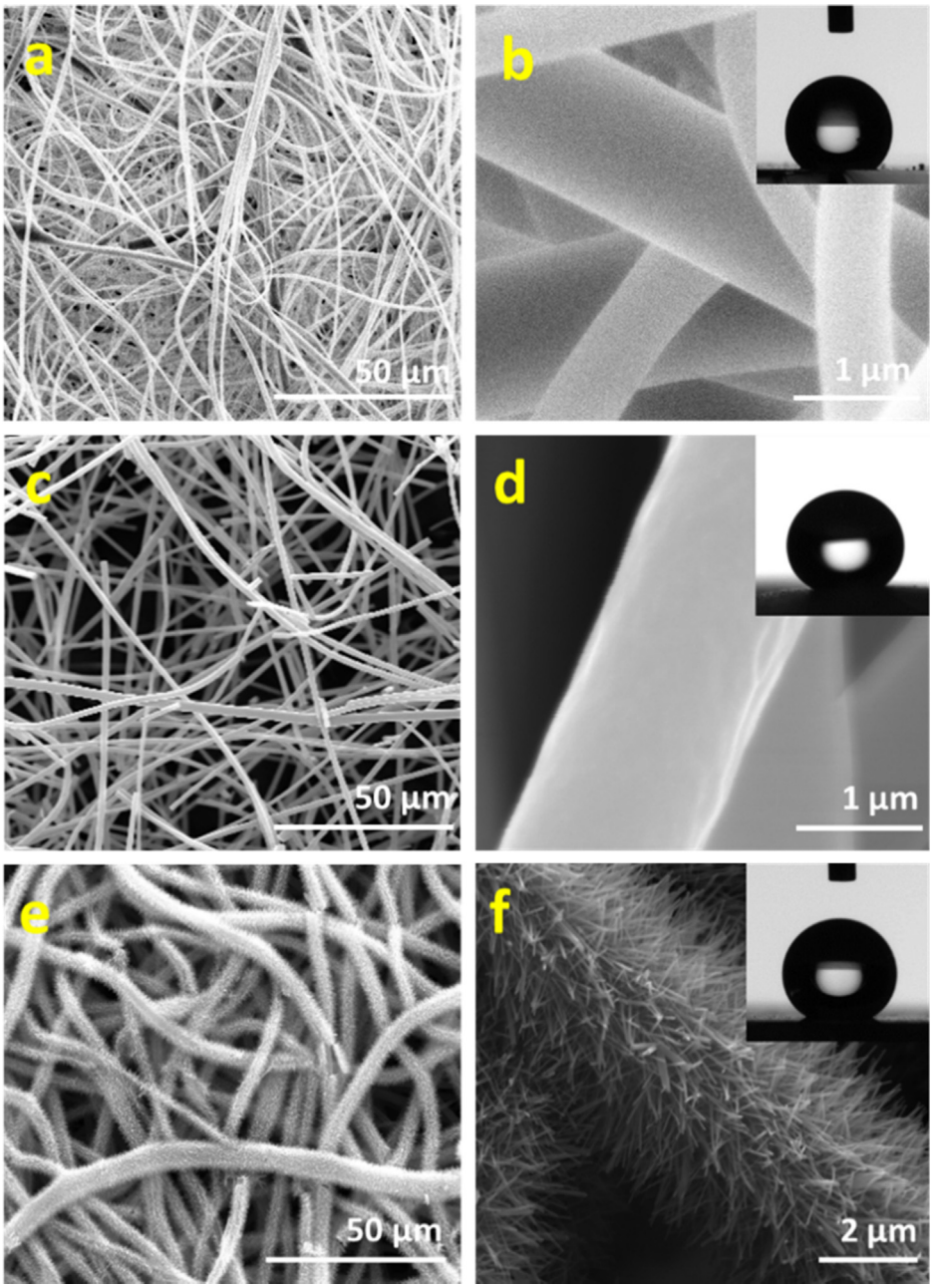

Fig. 2. Low- and high-magnification SEM images of the hierarchical HPIM nanofibrous web: SEM images of (a, b) pristine HPIM, (c, d) ALD-based ZnO-seeded HPIM, and (e, f) ZnO NR-decorated HPIM nanofibrous web.

on the HPIM surface, and no other peaks were detected, which confirmed the purity of the hierarchical network. Furthermore, the surface oxygen defect states and oxygen vacancies on the ZnO host lattice on the seed surface and the NR surface were quantified using the XPS spectra.

Fig. 5 displays the FT-IR spectra of the HPIM and ZnO-decorated HPIM nanofibrous membrane. The HPIM was stable after ZnO loading through ALD and after the solution growth process. The N—H vibration between 3500 and 3000 cm^{-1} and the carbonyl peaks associated with amide 1 and amide 2 at 1680 and 1590 cm^{-1} confirmed the complete hydrolysis of PIM-1 [41]. The structural features of the HPIM did not change after ALD and the solution growth process of ZnO. Moreover, the signal at around 430 cm^{-1} indicates the M–O stretching vibration results because of the presence of Zn–O on the HPIM surface [42]. Compared with that of the ZnO NR-HPIM nanofiber, the density of ZnO was low on the ZnO ALD-HPIM NFs, which resulted in the low M–O vibration on the HPIM surface. In addition, the broad peak centered at 3450 cm^{-1} was assigned to the stretching of hydrogen-bonded –OH groups on the nanostructures, which functionalized the HPIM surface.

The surface functionality was further confirmed by the XPS spectra of the pristine and ZnO-decorated HPIM nanofibers. The pristine nature of the HPIM with the additional ZnO functionality and the native oxygen defect states were determined for the hierarchical nanofibers (Fig. 6). As seen in the survey spectrum (Fig. 6a), the nitrogen functionality on the HPIM surface was stable after ZnO loading with the addition of some –Cl functionality due to the solvent effect. After the ZnO decoration, the resolved peak disappeared due to the cleaning process in the ZnO NR growth. Fig. 6b shows the high-resolution C 1 s spectra, with two major

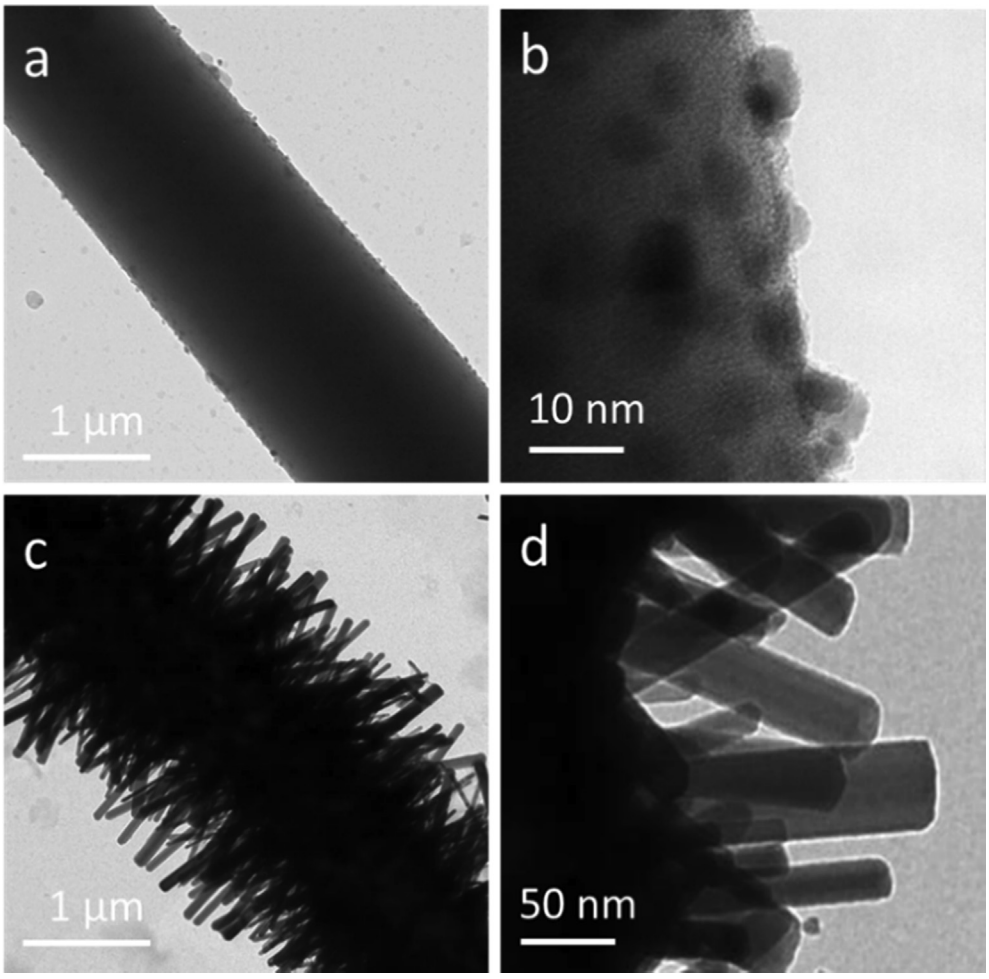

Fig. 3. Low- and high-magnification TEM images of the hierarchical HPIM nanofibrous web: (a, b) ALD-based ZnO-seeded HPIM nanofiber and (c, d) ZnO NR-decorated HPIM nanofiber.

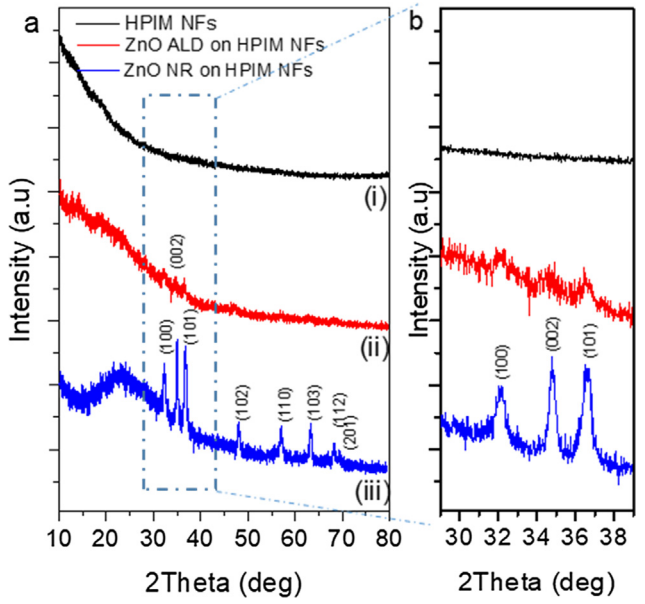

Fig. 4. XRD spectra of hierarchical HPIM nanofibrous web: (i) pristine HPIM, (ii) ALD-based ZnO-seeded HPIM, and (iii) ZnO NR-decorated HPIM nanofibrous web.

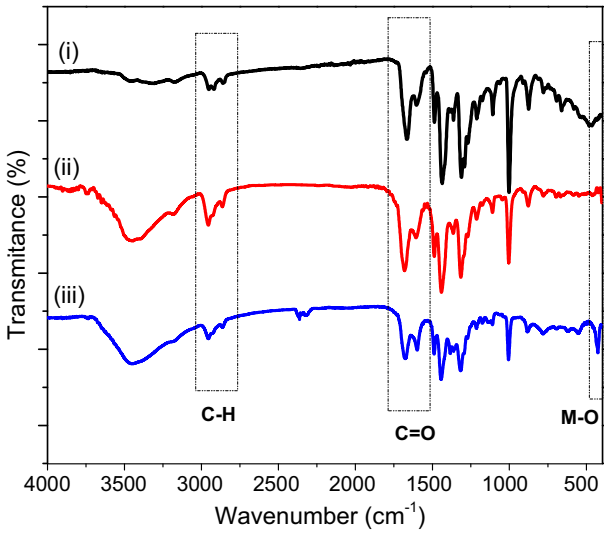

Fig. 5. FT-IR spectra of hierarchical HPIM nanofibrous web: (i) pristine HPIM, (ii) ALD-based ZnO-seeded HPIM, and (iii) ZnO NR-decorated HPIM nanofibrous web.

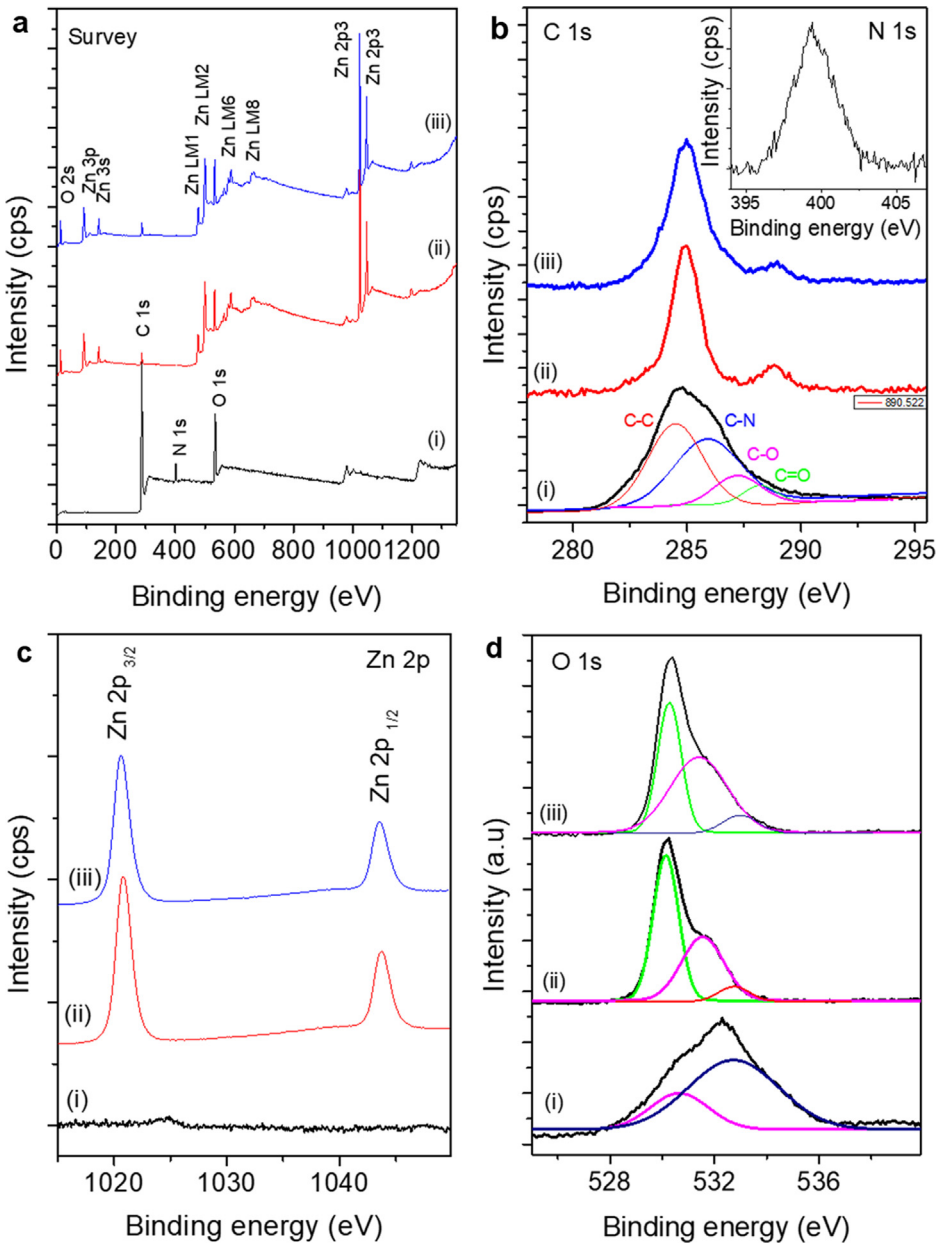

Fig. 6. XPS spectra of hierarchical HPIM nanofibrous web: (a) survey spectrum; (b) high-resolution C 1s spectra, wherein inset shows the high-resolution spectra of N 1s; (c) high-resolution Zn 2p spectra; and (d) high-resolution O 1s spectra. (i) HPIM NFs, (ii) ZnO ALD-HPIM NFs, and (iii) ZnO NR-HPIM NFs.

peaks at 284.6 eV and 288.4 eV, representing the C 1 s core level and oxygenated carbon, respectively [43]. The fibrous surface led to oxygen-containing functional groups such as the carboxyl and hydroxyl groups, which rationalized the broad peak at around 288.4 eV. The spectrum was deconvoluted into four peaks at binding energies of 284.6 (C—C), 285.4 (C—N), 286.7 (C—O), and 288.4 eV (C═O). Extended peaks for the pristine HPIM NFs, attributable to C—N, appeared at 285.4 eV on the fibrous surface [44]. The inset of Fig. 6b shows a N 1s signal at around 399 eV, attributable to the imidazole ring group on the HPIM fiber surface [45]. With the ZnO loading, the amount of N decreased due to the thermally induced growth process. Fig. 6c displays the high-resolution Zn 2p XPS spectra, showing two peaks at 1020.8 eV and 1043.9 eV, corresponding to Zn $2p_{3/2}$ and Zn $2p_{1/2}$ core levels, respectively [40]. The peak positions and distance between the peaks suggest the +2 oxidization state of ZnO on the fiber surface. To quantify the defect states on the ZnO seed layer and ZnO NRs, the high-resolution O 1s spectra were characterized and convoluted according to the surface functionality (Fig. 6d). The presence of oxygen defect states led to optical emission under visible irradiation, which promoted the photocatalytic activity. Over the HPIM surface, the hierarchical feature resulted in a wide and asymmetric peak representing multiple chemical states. Using the Gaussian function, the peaks were split into three according to oxidation states. The peak at 530.1 ± 0.2 eV denotes the lattice oxygen interacting with metal, which was similar for the ZnO seed layer and ZnO NR-decorated HPIM nanofiber surface [40,46]. The peaks at 531.2 ± 0.2 eV and 532.2 ± 0.2 eV denote oxygen vacancy/deficiency states and chemisorbed oxygen states on the ZnO-loaded fiber surface [40,46]. The pristine HPIM NFs exhibited two peaks assigned to oxygen functional groups at 530.8 ± 0.2 eV and 532.5 ± 0.2 eV, related to the C═O and O-C═O groups, respectively.

The UV DRS spectra (Fig. 7) reveal the characteristic absorption signal of the HPIM with the ZnO nanostructures. The strong signal

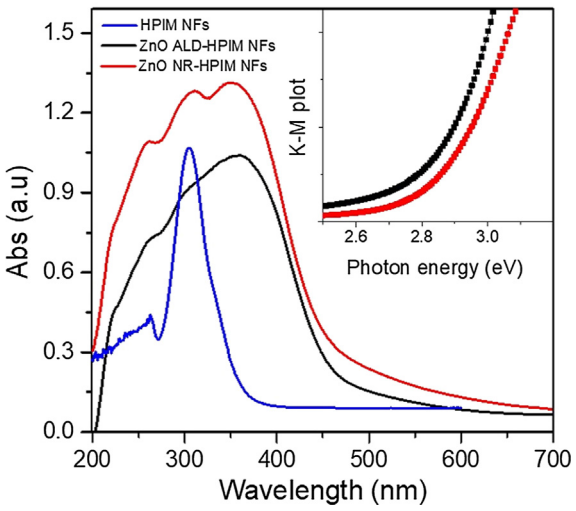

Fig. 7. UV–Vis DRS spectra of hierarchical HPIM nanofibrous web. Inset shows the K-M plot of the corresponding ZnO-decorated HPIM NFs.

with the sharp absorption edge at around 400 nm reveals the band edge emission of ZnO. The strong sub-band emission at the UV region at 300 nm represents the absorption of HPIM [24]. With the functionality of ZnO NR on the HPIM surface, the visible absorbance was extended to around 500 nm, which may be due to the presence of high oxygen-based defect states on the ZnO NR arrays. The possible presence of ZnO on the HPIM surface led to a shift in the band edge adsorption toward the visible region. The PL signal reveals the photoresponsive emission behavior of the HPIM nanofibers containing the ZnO functionality (Fig. S6). Under excitation at 340 nm, the strong emission at 380 nm represented the band edge emission of ZnO on the HPIM surface. Compared to that offered by the ZnO ALD seed layer, the band edge emission of ZnO was more intense, representing the loading density and crystalline nature of the ZnO on the HPIM surface. The broad emission in the visible region represents the surface functional emission of HPIM. With the function of ALD ZnO, the broad visible emission of HPIM shifted owing to the richness of oxygen interstitial states on the HPIM fiber surface. In the presence of ZnO NRs, two additional peaks were seen at around 460 nm and 500 nm, representing the oxygen-based vacancy states arising from ZnO NRs on the HPIM surface. The ZnO NR-grown HPIM fibers show promising band edge emission at 3.25 eV but there is only a trace signature of noted for the ZnO seed HPIM NFs. The relative spectral intensity of the band edge emission reveals the optical quality of the nanostructural platform. Similar to the ZnO seed layer, ZnO NR exhibited a significant broad emission in the visible region, which represents coupled relative emissions such as those of oxygen vacancy states [47]. The relative intensity of the band emission from the defect emission was nearly 10 times higher for the ZnO NR-grown HPIM fiber surface compared to the ALD-seeded HPIM NFs, which reveals the higher optical quality of the fibrous platform.

To evolve the selective adsorption and catalytic performance of the ZnO-decorated HPIM NF web over the contaminated water, MB-, RhB-, and MO-based dye molecules were used as typical organic pollutants. In the dark, under neutral conditions, the HPIM nanofibers showed an adsorption efficiency of 98.8%, 94.3%, and 3.3% for MB, RhB, and MO, respectively after 18 h and the ZnO NR-decorated HPIM nanofibers showed corresponding rates of 92.7%, 89.9%, and 8.1% (Fig. S7). The slight decrease in the absorption rate on the ZnO NR-decorated HPIM nanofibers were due to the changes in the surface charge and ZnO loading, which reduced the number of active HPIM adsorption sites. The highly electronegative functionality-containing HPIM-based nanofibers adsorbed nearly 90% of the cationic dyes such as MB and RhB (Fig. S7a, b), but barely adsorbed any MO dye in a similar period of time (only 8%) (Fig. S7c). Fig. S8 shows the change in color with respect to time in the presence of catalytic NFs. This trend was observed for both the pristine HPIM and ZnO-seeded HPIM nanofibers. Variation in the dye removal efficiency of the HPIM and ZnO NR-decorated HPIM NFs as a function of the pH was also investigated. Fig. 8a shows the effect of pH on MB and MO dye adsorption from aqueous solutions in the dark. The pH of the pollutant was varied from 3 to 11 at the adsorption concentration of 15 ppm with an adsorbate web size of 1 × 1 cm (~1.4 mg) and a contact time of 18 h. The HPIM NFs showed MB adsorption efficiencies of 49.1%, 65.3%, 86.7%, 98.1%, and 90.5% at pH 3, 5, 7, 9, and 11, respectively. For the ZnO NR-decorated HPIM NFs, the adsorption efficiencies were 47.1%, 62.7%, 83.4%, 92.7%, and 87.9% at pH 3, 5, 7, 8, and 10, respectively. Further, MO adsorption over at different pH showed that ZnO NR-HPIM NFs exhibited a 2.1–8.1% efficiency variation on varying the pH from 3 to 11, which resulted in a negative adsorption effect on the HPIM surface. The as-prepared HPIM nanofibers showed a high electronegativity of –62.2 mV under neutral conditions, which induced interactions with positivity charged ions, thereby facilitating cation adsorption on the fibrous surface. Increase in the pH led to the hybrid surfaces becoming more electronegative (Fig. S9), which favored the surface interactions with the cationic dye that promoted the adsorption and photodegradation efficiency. The effect of the contact time with the dye solution was studied under neutral pH by adding 1 × 1 cm^2 of adsorbent and 10 mL of the solution into special glass-stoppered tubes and the experiment was performed with the contact time varied from 0 to 18 h (Fig. 8b). The MB dye adsorption by the ZnO NR-HPIM nanofibers was slow and steady (Fig. 8b). At the contact time of 18 h, ZnO NR-HPIM nanofibers had attained adsorption equilibrium. Investigation of the kinetics of MB and MO dye removal through ZnO NR-HPIM NFs helped determine the adsorption behavior of the hierarchical fibrous web. Fig. S10 shows the adsorption rate of the dye molecules on the HPIM and ZnO NR-HPIM nanofibers. The kinetic data obtained for the adsorbent web could be better fitted to the pseudo-second-order kinetic model, suggesting chemical adsorption of the cationic pollutant by the HPIM surface. The HPIM-based fibrous surface did not participate in an active role in the adsorption of MO. Furthermore, the adsorption rate was much faster for the pristine HPIM and ZnO-seeded HPIM fibers compared to that noted for the ZnO NR-decorated HPIM NFs (Fig. S7d) due to the high surface interactions of HPIM in the fibrous morphology.

Fig. 8c and 8d exhibits the photodegradation rate of ZnO-loaded HPIM nanofibers over MB and MO under UV irradiation in neutral pH. In the presence of ZnO NR-decorated HPIM nanofibers, it took 18 h for the complete removal of MB in the dark. On the other hand, the dye solution reaches a decolorization efficiency of above 90% within 120 min under UV irradiation. After 100 min of UV irradiation, the photocatalytic degradation efficiency of HPIM, ZnO ALD-HPIM, and ZnO NR-HPIM NFs were 36.7%, 57.7%, and 94.1% respectively: the pristine HPIM NFs showed the lowest degradation performances resulting in the absence of photocatalytic activity. The results were compared with those previously reported for hybrid fibrous web-based catalytic networks, as summarized in Table S1. Compared to the commercially available ZnO (43.3% in 100 min), the hierarchical ZnO-loaded HPIM NFs displayed promising decolorization efficiency in a membrane form that offered simple recovery. The change in the decolorization efficiency was due to the effective photogenerated carrier on the ZnO surface leading to promotion of the radical ions and degradation of the adsorbed dye molecules on the HPIM surface, which further enhanced the adsorption. The faster degradation in the ZnO NR-HPIM NFs was due to the high electrostatic interactions of the cationic dye on

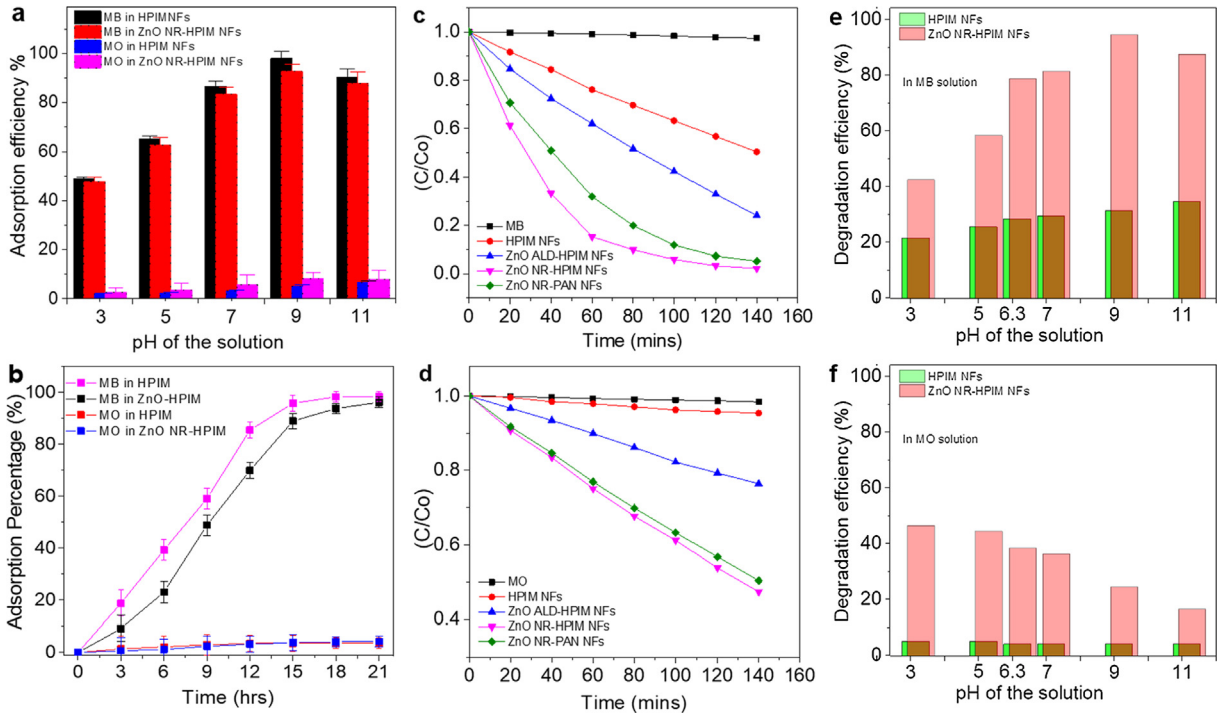

Fig. 8. Adsorption and photocatalytic properties of ZnO NR-decorated HPIM-based hierarchical NFs. (a) Effect of solution pH on adsorption in the dark (Dosage of adsorbent = 1 × 1 cm^2, concentration of metal ions = 15 mg L^{-1}, contact time = 120 min). (b) Effect of contact time on adsorption of MB and MO onto HPIM and ZnO NR-HPIM nanofibers in the dark. (Dosage of adsorbent = 1 × 1 cm^2, concentration of metal ions = 15 mg L^{-1}, pH = 6.0). (c, d) Photocatalytic efficiency for MB and MO against time, (e, f) pH-dependent catalytic efficiency of ZnO NR-HPIM NFs for MB and MO under 100 min of UV irradiation.

the fiber surface with simultaneous photodegradation activity of the high loading of ZnO nanostructures compared with that of ZnO ALD-HPIM NFs. In HPIM NFs, the decolorization efficiency was maintained only due to the surface adsorption of the cationic pollutant on the fiber surface. To understand the role of the selective adsorption sites in promoting the catalytic activity, the similar surface feature of ZnO NR decorated on polyacrylonitrile (PAN) NFs (Fig. S11) were compared. The ZnO NR-PAN NFs which has results 88.1% of degradation efficiency is slower than the ZnO ALD-HPIM NFs (94.1%) under similar time which results in fascinating surface adsorption effect of the HPIM fiber surface which facilitated faster catalytic activity. Fig. 8d shows that the photocatalytic degradation of MO had efficiencies of 4.1%, 23.6%, 50.2%, and 53.4% for the pristine HPIM, ZnO-seeded HPIM, ZnO NR-decorated PAN, and ZnO NR-decorated HPIM NFs. The degradation of MO was preferable due to the ZnO catalyst on the fiber surface, and HPIM nanofibers did not play any role in the photodegradation process and it did not adsorb any anionic dye molecules. The ZnO-decorated HPIM NFs showed superior degradation rate (Fig. S12) over the cationic pollutants under visible irradiation that was nearly 7 times higher than that of the HPIM NFs. This could be due to the fact that the HPIM nanofibers had a highly electronegative surface favoring the adsorption of cationic dyes on the surface, which led to the interactions of the dye with the catalyst surface being enhanced. To further confirm the byproduct formation during the photodegradation process, the degradation of MB dye molecules against time under visible irradiation with ZnO NR-decorated HPIM NFs was analyzed by LC-MS. Fig. S13 clearly shows the degradation of MB dye molecules without the formation of any byproducts after irradiation for 120 min using ZnO NR-decorated HPIM NFs as the catalyst. To address the significant promotional high electronegativity effect of the HPIM and ZnO surface, pH-dependent catalytic properties of the system over MB (Fig. 8e) and MO (Fig. 8f) were investigated using a series of solutions with pH ranging from 3.0 to 11.0 in degradation experiments. Compared to acidic conditions, the catalytic fibers showed a high degradation rate in basic pH. At neutral conditions, until pH 9, the degradation rate exhibited an incremental trend, and at pH 9 the degradation rate reached the maximum for MB. This may be due to the zero-point energy of ZnO and the deprotonation effect of HPIM, resulting in effective surface interactions of the MB dye with ZnO and HPIM at that pH which facilitated faster degradation [25,47]. At basic conditions above pH 9, the surface of ZnO became negatively charged (higher than zero-point energy of ZnO) and facilitated the adsorption of more cationic dyes to the catalyst surface and enhanced the catalytic activity. Under strongly alkaline environments (pH ≥ 11), ZnO may undergo dissolution due to the high OH functionality that could slow the degradation rate [48]. Compared to pristine HPIM NFs and ZnO-seeded HPIM NFs, ZnO NR-decorated HPIM showed a faster degradation due to the photogenerated charge carrier on the ZnO-loaded HPIM surface. The effective density of the ZnO NR led to higher catalytic activity compared to the ALD-grown ZnO nanograins on the HPIM NF surface. However, the degradation of MO with respect to the pH was reversible unlike that of MB. This phenomenon was due to the dyes and the surface-charge properties of the photocatalysts, which are related to the zero charge. Since MO is an anionic dye, in acidic conditions, electrostatic interactions between the anionic dyes and positively charged catalyst improve the degree of adsorption, which favors the photocatalytic activity; however, under basic conditions, electrostatic repulsion results in poor catalytic efficiency [49]. The reusability and stability of the catalytic web was investigated to demonstrate the promising lifetime of the catalytic web. The reusability of the catalytic web when used for MB under neutral conditions (pH 6.3) was performed by reusing the catalytic web for multiple catalytic cycles (Fig. 9a) for 150 min of photoirradiation for each cycle. The results suggested successful reuse for ten consecutive catalytic cycles with a conversion of >90%, demonstrating the excellent recyclability of the catalytic

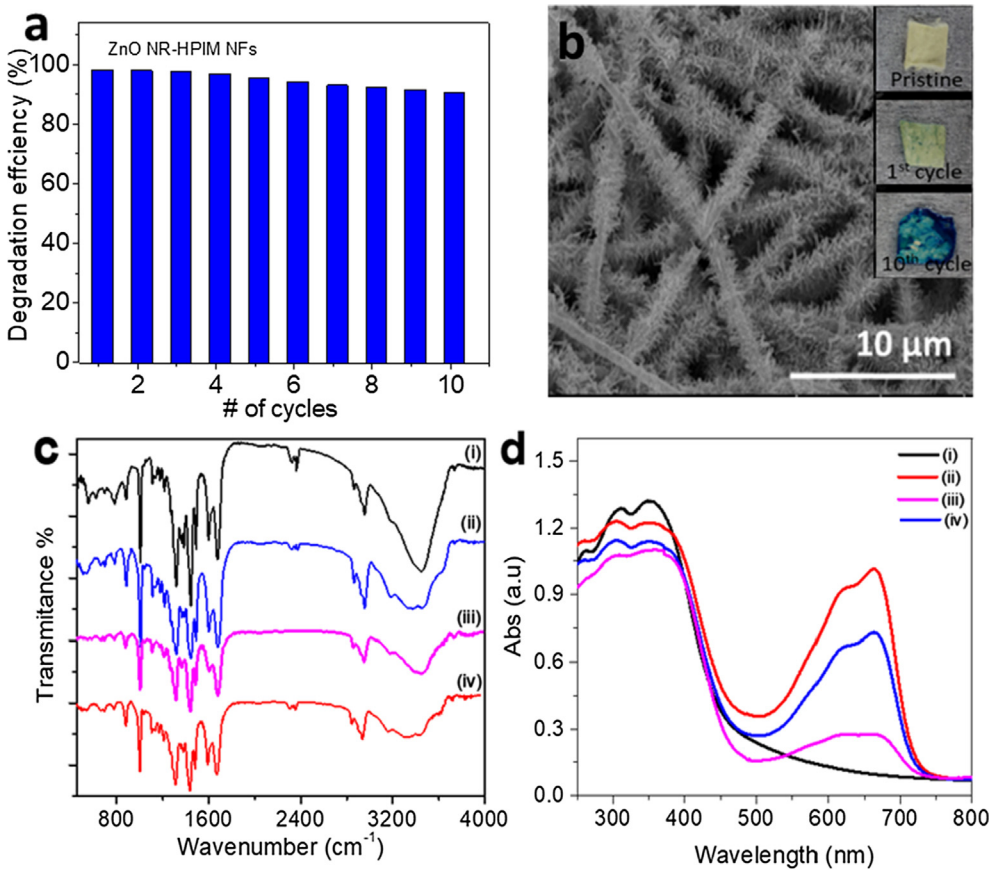

Fig. 9. Reusability and dye-adsorbing functionality of hierarchical webs. (a) Photocatalytic reusable properties of the hierarchical fibrous web over MB; (b) SEM images of ZnO NR-decorated HPIM NFs after ten photodegradation cycles: the inset shows the effect of dye loading on catalytic webs; (c, d) FT-IR and UV–Vis DRS spectra of the hierarchical catalytic web (i) in pristine ZnO NR-HPIM NFs, (ii) ZnO NR-HPIM NFs after MB dye adsorption in dark, (iii) simultaneous MB adsorption & degradation under UV on ZnO NR-HPIM NFs, (iv) reused ZnO NR-HPIM NFs photocatalyst after 10 cycles of MB degradation.

web. Moreover, the stability of the catalyst was demonstrated by morphological characterization using SEM images. The hierarchical ZnO-HPIM NFs assembly was stable after multiple catalytic cycles (Fig. 9b). The inset of Fig. 9b shows the optical images of the ZnO-decorated HPIM NFs before and after ten cycles, displaying the stability of the 3D hierarchical web surface.

Since the HPIM NF exhibited effective adsorption through chemical interactions with cationic pollutants, reversible swell of the adsorbed pollutants was quite difficult with the water. However, the slow and steady adsorption of cationic dye on the ZnO NR-HPIM surface led to degradation of the surface-adsorbed dye molecules effectively under photoirradiation and resulted in faster degradation. During multiple uses, the fibrous web started to adsorb the cationic pollutants to its core surface, which minimized the possibility of the photogenerated carrier to degrade the dye molecules that reached the core of the HPIM nanofibers (inset, Fig. 9b: dye-adsorbed fibers). PIM-1 has exhibited the reversible swell of its absorbed pollutants in the presence of methanol [24]. After immersing the dye-adsorbed ZnO NR-HPIM NFs in methanol-mixed water (1:9), 60% of its dye-adsorbed functionality was confirmed to have been lost, as confirmed by the UV DRS spectra of the dye-absorbed ZnO-HPIM NFs (Fig. 9d). The lower desorption rate was due to the strong interaction of cationic dyes with the highly electronegative HPIM surfaces and because the dye molecule was adsorbed to the core fiber surface, which did not interact with the ZnO surface to get degraded. Without the methanol, the desorption rate was further delayed because of the strong adsorption of the dye on the HPIM NFs. Methanol dissolved the dye from the core fiber for effective participation in the photocatalytic degradation process on the fiber surface. As in semiconducting catalysis, the surface interaction mainly resulted in faster interaction of the dye molecules with the photogenerated reactive oxygen species (ROS), which produced at the catalytic surface [50]. The pristine HPIM did not show any significant change under the photoirradiation and MB was not degraded or leached from its surface. However, in ZnO-loaded HPIM NFs, surface-decorated ZnO NR could produce more superoxide radicals (Fig. S14) under photoirradiation and promote the photodegradation, which only left a mild trace of dye functionality on the catalytic fiber surface. Additionally, the FT-IR spectrum (Fig. 9c) of the ZnO NR-HPIM NFs before and after the catalytic process revealed that there was not much dye functionality on the NF surface after the degradation process, which meant effective degradation of dye molecules under the photocatalytic process. To quantify the dye loading density, the pristine and dye-degraded nanofibrous web were compared with the dye-absorbed HPIM NF web, which exhibited a lower density of carbon functionalities, close to that of the pristine HPIM surface: this led to the nearly complete degradation of dye molecules on HPIM surface under photoirradiation.

Further, to evaluate the selectivity towards the pollutant molecules in mixed samples, such as the mixtures MB and MO, MO and RhB, and MB and RhB were prepared and investigated by ZnO NR-decorated HPIM NFs catalyst in the dark and under UV irradiation (Fig. 10). The UV–Vis absorbance spectral intensity against the wavelength of the dye molecules determined the adsorption capability of the catalytic fibers. Fig. 10a, c, e show the UV absorbance

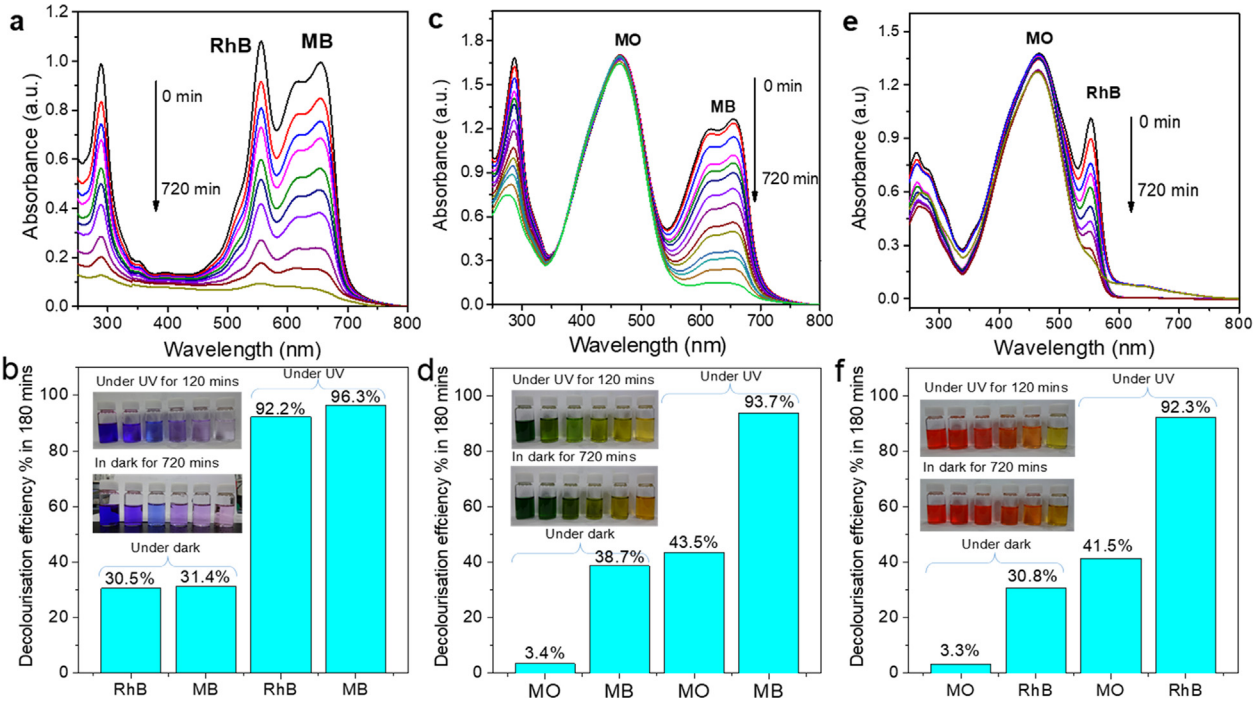

Fig. 10. Selective adsorption and degradation of hierarchical webs towards mixed dyes: UV absorbances spectra of mixed dyes with ZnO NR-decorated HPIM NFs in dark for 720 min: (a) MB and RhB, (c) MB and MO, and (e) RhB and MO. (b, d, f) Adsorption and degradation efficiencies in the dark and under UV irradiation in mixed dye solutions in 180 min, respectively. Insert shows the color change of the mixed dyes solution in the dark and under UV irradiation against time containing ZnO NR-decorated HPIM nanofibrous web.

spectra of the mixed dye solutions kept with the ZnO NR-decorated HPIM NFs in the dark against time. The results illustrated the effective adsorption of the cationic dyes such as MB and RhB since their respective absorbance peaks disappeared, with only the characteristic anionic dye (MO) absorbance peaks being detected in the dye mixture (Fig. 10a, c, e). The photographs of the dye solution obtained at various times show the change in color from green to purple to colorless for mixed MB-RhB, orange from mixed for MB-MO, and red to orange for the mixed MO-RhB, as can be observed by the naked eye (inset of Fig. 10), respectively. The results demonstrate high selectivity towards the cationic pollutant and that simultaneous UV irradiation led to faster degradation on the ZnO NR-decorated HPIM NFs.

The superior degradation performances over the hierarchical ZnO NR-decorated HPIM NF surface were attributable to (i) the strategical effect of the highly electronegative functionality of the ZnO and HPIM NFs, which led to selective adsorption and following degradation of cationic pollutants; (ii) the promotional effect of highly dense ZnO NRs, which offered richness of ROS on the fiber surface that degraded the surface-absorbed pollutants; (iii) faster degradation of surface-adsorbed pollutants by the ZnO NRs leading to further adsorption of the pollutant from the reactant solution, which positively affected the high degradation rate; (iv) the solution growth of ZnO NRs inducing richness of oxygen defect states that minimized the recombination rate and promoted the photogenerated electron to the catalytic surface to enhance the catalytic activity. (v) the network assembly of the 3D web-based fiber surface inducing a high surface area and exposing the rich active sites as well as favoring multiple cycles of use. The hierarchical fibrous membrane is highly selective towards cationic dyes and shows promising catalytic activity towards cationic dye molecules. The pristine NFs showed decreased adsorption capacity after multiple cycles. However, ZnO-decorated HPIM fibers showed promising adsorption of dye due to the degradation process, which offered a platform to adsorb the pollutant again and again without destroying its morphology.

4. Conclusions

In summary, ZnO-decorated HPIM NFs were successfully synthesized through aqueous solution-grown ZnO NRs on electrospinning of HPIM with the promotional nucleation effect by ALD-grown ZnO on the HPIM surface. These hierarchical fibers were adopted for the selective dye adsorption-cum-degradation of mixed textile dye solutions under photoirradiation. The HPIM surface exhibited selectivity toward the adsorption of cationic dye molecules (MB and RhB) and the ZnO effectivity degraded the dye molecules under photoirradiation. The adsorption functionality on the HPIM surface led to favorable interactions of pollutant molecules on the catalyst surface, which improved the catalytic rate through feasible surface interactions. Further, the synthetic process formed a stable structure and morphology that were retained after several cycles of use, suggesting low leaching of ZnO and excellent reusable performance. This work thus demonstrates the easy fabrication of flexible freestanding hierarchical nanofibrous membranes towards selective degradation of pollutants in dye solutions with reusability and high stability.

Declaration of Competing Interest

The authors declare that they have no known competing financial interests or personal relationships that could have appeared to influence the work reported in this paper.

Acknowledgments

K. S. Ranjith acknowledges The Scientific & Technological Research Council of Turkey (TUBITAK), BIDEB 2216-Fellowships for Research Fellowship Programme for Foreign Citizens) for a postdoctoral fellowship. The authors thank Dr. Bhushan Patil and Sefika Ozcan for performing XRD and PL. We acknowledge financial support from the Basic Science Research Program through the

National Research Foundation of Korea (NRF) funded by the Ministry of Science, ICT & Future Planning (2019R1F1A1061477).

Appendix A. Supplementary material

Supplementary data to this article can be found online at https://doi.org/10.1016/j.jcis.2019.11.096.

References

[1] M.T. Amin, A.A. Alazba, U. Manzoor, A review of removal of pollutants from water/wastewater using different types of nanomaterials, Adv. Mater. Sci. Eng. 825910 (2014), https://doi.org/10.1155/2014/825910.

[2] N.A. Awang, W.N. Wan Salleh, A.F. Ismail, N. Yusof, F. Aziz, J. Jaafar, Adsorption behavior of chromium(vi) onto regenerated cellulose membrane, Ind. Eng. Chem. Res., 58 (2019) 720–728, https://doi.org/10.1021/acs.iecr.8b02366.

[3] Y. Fang, Q. Huang, P. Liu, J. Shi, G. Xu, A facile dip-coating method for the preparation of separable MoS_2sponges and their high-efficient adsorption behaviors of Rhodamine B, Inorg. Chem. Front. 5 (2018) 827–834, https://doi.org/10.1039/C8QI00012C.

[4] S. Gita, S.P. Shukla, N. Saharan, C. Prakash, G. Deshmukh, Toxic effects of selected textile dyes on elemental composition, photosynthetic pigments, protein content and growth of a freshwater chlorophycean alga chlorella vulgaris, Bull. Environ. Contam. Toxicol. 102 (2019) 795–801, https://doi.org/10.1007/s00128-019-02599-w.

[5] A.D. Levine, T. Asano, Peer reviewed: recovering sustainable water from wastewater, Environ. Sci. Technol. 38 (2004) 201A–208A, https://doi.org/10.1021/es040504n.

[6] Z. Wang, A. Wu, L.C. Ciacchi, G. Wei, Recent advances in nanoporous membranes for water purification, Nanomaterials 8 (2018) 65, https://doi.org/10.3390/nano8020065.

[7] Y. Yang, P. Dementy, N. Biere, D. Emmrich, P. Stohmann, R. Korzetz, X. Zhang, A. Beyer, S. Koch, D. Anselmetti, A. Gölzhäuser, Rapid water permeation through carbon nanomembranes with sub-nanometer channels, ACS Nano 125 (2018) 4695–4701, https://doi.org/10.1021/acsnano.8b01266.

[8] V.V. Kadam, L. Wang, R. Padhye, Electrospun nanofibre materials to filter air pollutants – a review, J. Ind. Text. 47 (2018) 2253–2280, https://doi.org/10.1177/1528083716676812.

[9] M.M. Khin, A.S. Nair, V. Jagadeesh Babu, R. Murugan, S. Ramakrishna, A review on nanomaterials for environmental remediation, Energy Environ. Sci. 5 (2012) 8075–8109, https://doi.org/10.1039/C2EE21818F.

[10] D. Li, H. Baydoun, C.N. Verani, S.L. Brock, Efficient water oxidation using CoMnP nanoparticles, J. Am. Chem. Soc. 138 (2016) 4006–4009, https://doi.org/10.1021/jacs.6b01543.

[11] L. Luo, L. Zhang, Z. Duan, A.S. Lapp, G. Henkelman, R.M. Crooks, Efficient CO oxidation using dendrimer-encapsulated pt nanoparticles activated with <2% Cu surface atoms, ACS Nano 10 (2016) 8760–8769, https://doi.org/10.1021/acsnano.6b04448.

[12] L. Wang, G. Hu, Z. Wang, B. Wang, Y. Song, H. Tang, Highly efficient and selective degradation of methylene blue from mixed aqueous solution by using monodisperse $CuFe_2O_4$ nanoparticles, RSC Adv. 5 (2015) 73327–73332, https://doi.org/10.1039/C5RA10543A.

[13] L.H. Li, J. Xiao, P. Liu, G.W. Yang, Super adsorption capability from amorphousization of metal oxide nanoparticles for dye removal, Sci. Rep. 5 (2015) 9028, https://doi.org/10.1038/srep09028.

[14] Z. Ajji, A.M. Ali, Adsorption of methyl violet and brilliant blue onto poly(vinyl alcohol) membranes grafted with N-vinyl imidazole/acrylic acid, Nucl. Instrum. Methods Phys. Res. Sect. B. 265 (2007) 362–365, https://doi.org/10.1016/j.nimb.2007.09.004.

[15] T. Wang, D. Wang, H. Zhang, X. Wang, M. Chen, Laser-induced convenient synthesis of porous Cu_2O@CuO nanocomposites with excellent adsorption of methyl blue solution, Optical Mater. Express 7 (2017) 924–931, https://doi.org/10.1364/OME.7.000924.

[16] M.G. Peleyeju, O.A. Arotiba, Recent trend in visible-light photoelectrocatalytic systems for degradation of organic contaminants in water/wastewater, Environ. Sci. Water Res. Technol. 4 (2018) 1389–1411, https://doi.org/10.1039/C8EW00276B.

[17] C.C. Wang, J.R. Li, X.L. Li, Y.Q. Zhang, G. Guo, Photocatalytic organic pollutants degradation in metal-organic frameworks, Energy Environ. Sci. 7 (2014) 2831–2867, https://doi.org/10.1039/C4EE01299B.

[18] S. Chang, X. Yang, Y. Sang, H. Liu, Highly efficient photocatalysts and continuous-flow photocatalytic reactors for degradation of organic pollutants in wastewater, Chem. Asian J. 11 (2016) 2352–2371, https://doi.org/10.1002/asia.201600363.

[19] Y.H. Chiu, T.M. Chang, C.Y. Chen, M. Sone, Y.J. Hsu, Mechanistic insights into photodegradation of organic dyes using heterostructure photocatalysts, Catalysts 9 (2019) 430, https://doi.org/10.3390/catal9050430.

[20] H. Chun, W. Yizhong, T. Hongxiao, Influence of adsorption on the photodegradation of various dyes using surface bond conjugated TiO_2/SiO_2 photocatalyst, Appl. Catal. B Environ. 35 (2001) 95–105, https://doi.org/10.1016/S0926-3373(01)00236-3.

[21] N. Zhang, Y. Zhang, Y.J. Xu, Recent progress on graphene-based photocatalysts: current status and future perspectives, Nanoscale 4 (2012) 5792–5813, https://doi.org/10.1039/C2NR31480K.

[22] S.P. Lonkar, V.V. Pillai, S.M. Alhassan, Facile and scalable production of heterostructured ZnS-ZnO/Graphene nano-photocatalysts for environmental remediation, Sci. Rep. 8 (2018) 13401, https://doi.org/10.1038/s41598-018-31539-7.

[23] L. Di, H. Yang, T. Xian, X. Chen, Construction of Z-scheme g-C_3N_4/CNT/$Bi_2Fe_4O_9$ composites with improved simulated-sunlight photocatalytic activity for the dye degradation, Micromachines 9 (2018) 613, https://doi.org/10.3390/mi9120613.

[24] B. Satilmis, P.M. Budd, T. Uyar, Systematic hydrolysis of PIM-1 and electrospinning of hydrolyzed PIM-1 ultrafine fibers for an efficient removal of dye from water React, Funct. Polym. 121 (2017) 67–75, https://doi.org/10.1016/j.reactfunctpolym.2017.10.019.

[25] B. Satilmis, P.M. Budd, Selective dye adsorption by chemically-modified and thermally-treated polymers of intrinsic microporosity, J. Colloid Interface Sci. 492 (2017) 81–91, https://doi.org/10.1016/j.jcis.2016.12.048.

[26] B. Satilmis, T. Isik, M.M. Demir, T. Uyar, Amidoxime functionalized polymers of intrinsic microporosity (PIM-1) electrospun ultrafine fibers for rapid removal of uranyl ions from water, Appl Surf. Sci. 467–468 (2019) 648–657, https://doi.org/10.1016/j.apsusc.2018.10.210.

[27] B. Satilmis, T. Uyar, Development of superhydrophobic electrospun fibrous membrane of polymers of intrinsic microporosity (PIM-2), Eur. Polym. J. 112 (2019) 87–94, https://doi.org/10.1016/j.eurpolymj.2018.12.029.

[28] B. Satilmis, T. Uyar, Amine modified electrospun PIM-1 ultrafine fibers for an efficient removal of methyl orange from an aqueous system, Appl. Surf. Sci. 453 (2018) 220–229, https://doi.org/10.1016/j.apsusc.2018.05.069.

[29] B. Satilmis, T. Uyar, Superhydrophobic hexamethylene diisocyanate modified hydrolyzed polymers of intrinsic microporosity electrospun ultrafine fibrous membrane for the adsorption of organic compounds and oil/water separation, ACS Appl. Nano Mater. 1 (2018) 1631–1640, https://doi.org/10.1021/acsanm.8b00115.

[30] P. Mishra, S. Patnaik, K. Parida, An overview of recent progress on noble metal modified magnetic Fe_3O_4 for photocatalytic pollutant degradation and H_2 evolution, Catal. Sci. Technol. 9 (2019) 916–941, https://doi.org/10.1039/C8CY02462F.

[31] R. Chalasani, S. Vasudevan, Cyclodextrin-functionalized Fe_3O_4@TiO_2: reusable, magnetic nanoparticles for photocatalytic degradation of endocrine-disrupting chemicals in water supplies, ACS Nano 7 (2013) 4093–4104, https://doi.org/10.1021/nn400287k.

[32] K.S. Ranjith, A. Celebioglu, H. Eren, N. Biyikli, T. Uyar, Monodispersed, highly interactive facet (111)-oriented Pd nanograins by ALD onto free-standing and flexible electrospun polymeric nanofibrous webs for catalytic application, Adv. Mater. Interf. 4 (2017) 1700640, https://doi.org/10.1002/admi.201700640.

[33] A. Celebioglu, S. Ipek, E. Durgun, T. Uyar, Selective and efficient removal of volatile organic compounds (VOCs) by channel-type gamma-cyclodextrin assembly thru inclusion complexation, Ind. Eng. Chem. Res. 56 (2017) 7345–7354, https://doi.org/10.1021/acs.iecr.7b01084.

[34] A. Senthamizhan, A. Celebioglu, T. Uyar, Ultrafast on-site selective visual detection of TNT at Sub ppt level using single nanofiber incorporating fluorescent gold cluster, Chem Comm. 51 (2015) 5590, https://doi.org/10.1039/C4CC01190B.

[35] Mianli Huang, Sunxian Weng, Bo Wang, Hu. Jun, Fu. Xianzhi, Ping Liu, Various facet tunable ZnO crystals by a scalable solvothermal synthesis and their facet-dependent photocatalytic activities, J. Phy. Chem. C 118 (2014) 25434–25440, https://doi.org/10.1021/jp5072567.

[36] Zengxia Pei, Luyao Ding, Hu Jun, Sunxian Weng, Zuyang Zheng, Mianli Huang, Ping Liu, Defect and its dominance in ZnO films: a new insight into the role of defect over photocatalytic activity, Appl. Catal. B 142 (2013) 736–743, https://doi.org/10.1016/j.apcatb.2013.05.055.

[37] Martina Ussia, Alessandro Di Mauro, Tommaso Mecca, Francesca Cunsolo, Giuseppe Nicotra, Corrado Spinella, Pierfrancesco Cerruti, Giuliana Impellizzeri, Vittorio Privitera, Sabrina C. Carroccio, ZnO–pHEMA nanocomposites: an ecofriendly and reusable material for water remediation, ACS Appl. Mater. Interface 10 (2018) 40100–40110, https://doi.org/10.1021/acsami.8b13029.

[38] F. Kayaci, S. Vempati, C.O. Akgun, N. Biyikli, T. Uyar, Enhanced photocatalytic activity of homoassembled ZnO nanostructures on electrospun polymeric nanofibers: a combination of atomic layer deposition and hydrothermal growth, Appl. Catal. B 156–157 (2014) 173–183, https://doi.org/10.1016/j.apcatb.2014.03.004.

[39] B. Satilmis, T. Uyar, Removal of aniline from air and water by polymers of intrinsic microporosity (PIM-1) electrospun ultrafine fibers, J. Colloid Interface Sci. 516 (2018) 317–324, https://doi.org/10.1016/j.jcis.2018.01.069.

[40] K.S. Ranjith, R.B. Castillo, M. Sillanpaa, R.T. Rajendra Kumar, Effective shell wall thickness of vertically aligned ZnO-ZnS core-shell nanorod arrays on visible photocatalytic and photo-sensing properties, Appl. Catal. B 237 (2018) 128–139, https://doi.org/10.1016/j.apcatb.2018.03.099.

[41] B. Satilmis, T. Uyar, Fabrication of thermally crosslinked hydrolyzed polymers of intrinsic microporosity (HPIM)/polybenzoxazine electrospun nanofibrous membranes, Macromol. Chem. Phys. 220 (2019) 1800326, https://doi.org/10.1002/macp.201800326.

[42] S. Dong, Y. Li, J. Sun, C. Yu, Y. Li, J. Sun, Facile synthesis of novel ZnO/RGO hybrid nanocomposites with enhanced catalytic performance for visible-light-driven photodegradation of metronidazole, Mater. Chem. Phys. 145 (2014) 357–365, https://doi.org/10.1016/j.matchemphys.2014.02.024.

[43] S.H. Patil, A.P. Gaikwad, S.D. Sathaye, K.R. Patil, To form layer by layer composite film in view of its application as supercapacitor electrode by exploiting the techniques of thin films formation just around the corner, Electrochim. Acta 265 (2018) 556–568, https://doi.org/10.1016/j.electacta.2018.01.165.
[44] S. Yuan, J. Gu, Y. Zheng, W. Jiang, B. Liang, S.O. Pehkonen, Purification of phenol-contaminated water by adsorption with quaternized poly (dimethylaminopropyl methacrylamide)-grafted PVBC microspheres, J. Mater. Chem. A 3 (2015) 4620–4636, https://doi.org/10.1039/C4TA06363E.
[45] S. Ding, Z. Li, Y. Cheng, C. Du, J. Gao, Y.W. Zhang, N. Zhang, Z. Li, N. Chang, X. Hu, Enhancing adsorption capacity while maintaining specific recognition performance of mesoporous silica: a novel imprinting strategy with amphiphilic ionic liquid as surfactant, Nanotechnology 29 (2018) 375604, https://doi.org/10.1088/1361-6528/aace10.
[46] K.S. Ranjith, A. Senthamizhan, B. Balusamy, T. Uyar, Nanograined surface shell wall controlled ZnO–ZnS core–shell nanofibers and their shell wall thickness dependent visible photocatalytic properties, Catal. Sci. Technol. 7 (2017) 1167–1180, https://doi.org/10.1039/C6CY02556K.
[47] K.S. Ranjith, R.T. Rajendra Kumar, Surfactant free, simple, morphological and defect engineered ZnO nanocatalyst: Effective study on sunlight driven and reusable photocatalytic properties, J Photochem. Photobiol. 329 (2016) 35–45, https://doi.org/10.1016/j.jphotochem.2016.06.014.
[48] W. Raza, S.M. Faisal, Mohammad Owais, D. Bahnemann, M. Muneer, Facile fabrication of highly efficient modified ZnO photocatalyst with enhanced photocatalytic, antibacterial and anticancer activity, RSC Adv. 6 (2016) 78335–78350, https://doi.org/10.1039/c6ra06774c.
[49] X. Chen, Z. Wu, D. Liu, Z. Gao, Preparation of ZnO photocatalyst for the efficient and rapid photocatalytic degradation of azo dyes, Nanoscale Res Lett. 12 (2017) 143, https://doi.org/10.1186/s11671-017-1904-4.
[50] Y. Li, W. Zhang, J. Niu, Y. Chen, Mechanism of photogenerated reactive oxygen species and correlation with the antibacterial properties of engineered metal-oxide nanoparticles, ACS Nano 6 (2012) 5164–5173, https://doi.org/10.1021/nn300934k.